





Programmable order by disorder effect and underlying phases through dipolar quantum simulators

Huan-Kuang Wu ¹, Takafumi Suzuki ², Naoki Kawashima ^{3,4} and Wei-Lin Tu ^{5,*}

¹*Department of Physics, Condensed Matter Theory Center and Joint Quantum Institute, University of Maryland, College Park, Maryland 20742, USA*

²*Graduate School of Engineering, University of Hyogo, Hyogo, Himeji 670-2280, Japan*

³*Institute for Solid State Physics, University of Tokyo, Kashiwa, Chiba 277-8581, Japan*

⁴*Trans-scale Quantum Science Institute, The University of Tokyo, Bunkyo, Tokyo 113-0033, Japan*

⁵*Faculty of Science and Technology, Keio University, 3-14-1 Hiyoshi, Kohoku-ku, Yokohama 223-8522, Japan*



(Received 11 October 2023; accepted 21 May 2024; published 20 June 2024)

In this work, we study two different quantum simulators composed of molecules with dipole-dipole interaction through various theoretical and numerical tools. Our first result provides knowledge of the quantum order by disorder effect of the $S = 1/2$ system, which is programmable in a quantum simulator composed of circular Rydberg atoms in the triangular optical lattice with a controllable diagonal anisotropy. When the numbers of up spins and down spins are equal, a set of subextensive degenerate ground states is present in the classical limit, composed of continuous strings whose configuration enjoys a large degree of freedom. Among all possible configurations, we focus on the stripe (up and down spins aligning straightly) and kinked (up and down spins forming zigzag spin chains) patterns. Adopting the real space perturbation theory, we estimate the leading order energy correction when the nearest-neighbor spin exchange coupling, J , is considered, and the overall model becomes an effective XXZ model with a spatial anisotropy. Our calculation demonstrates a lifting of the degeneracy, favoring the stripe configuration. When J becomes larger, we adopt the infinite projected entangled-pair state (iPEPS) and numerically check the effect of degeneracy lifting. The iPEPS results show that even when the spin exchange coupling is strong the stripe pattern is still favored. Next, we study the dipolar bosonic model with tilted polar angle which can be realized through a quantum simulator composed of cold atomic gas with dipole-dipole interaction in an optical lattice. By placing the atoms in a triangular lattice and tilting the polar angle, the diagonal anisotropy can also be realized in the bosonic system. With our cluster mean-field theory calculation, we provide various phase diagrams with different tilted angles, showing the abundant underlying phases including the supersolid. Our proposal indicates realizable scenarios through quantum simulators in studying the quantum effect as well as extraordinary phases. We believe that our results indicated here can also become a good benchmark for two-dimensional quantum simulators.

DOI: [10.1103/PhysRevResearch.6.023297](https://doi.org/10.1103/PhysRevResearch.6.023297)

I. INTRODUCTION

Quantum many-body systems are often represented by a Hamiltonian whose composing parts do not commute with each other. This suggests that although the properties of low-energy states can be easily identified in a certain limit, often referred to as the classical limit, considering the whole Hamiltonian will make the estimation of the ground state difficult because one needs to consider the superposition of every state in the full Hilbert space. Moreover, the extra quantum or even thermal effect may lead to further stabilization among some competing low-energy states, causing energy level crossing or degeneracy lifting, known as the order by disorder (OBD) effect [1–22]. Besides, the introduction of

frustration, through the Hamiltonian [23–26] or lattice geometry [27–32], can also result in the manifold degeneracy of the ground state in the classical picture, and such degeneracy enriches the quantum or thermal fluctuation.

Among all structures, the triangular lattice is the simplest lattice structure for inducing geometrical frustration. Particularly, the inclusion of anisotropy could lead to the formation of long strings composed of the same spins [33]. The shape of strings enjoys a great degree of freedom, leading to a manifold degeneracy. Classically, such systems and their degeneracies can be realized, as a composition of self-assembled colloidal particles in a monolayer [34,35]. For this soft-matter system, particles move to the opposite walls that confine them to maximize the free volume, corresponding to the up-and-down spin scenario and forming a good platform for studying the dynamics of frustration. In d dimensions, the entropy of degenerate ground states is proportional to L^{d-1} , with the number of sites $N \sim L^d$, resulting in a subextensive degeneracy. For the above-mentioned frustrated colloidal system, its thermal OBD effect has been studied [36] and the authors unveiled the conclusion that the straight stripe should be favored. On the other hand, the quantum counterpart for such

*Contact author: weilintu@keio.jp

Published by the American Physical Society under the terms of the [Creative Commons Attribution 4.0 International license](https://creativecommons.org/licenses/by/4.0/). Further distribution of this work must maintain attribution to the author(s) and the published article's title, journal citation, and DOI.

OBD effect at zero temperature is also of interest. When an extra noncommutable term, such as the spin exchange coupling, is introduced to the Ising-like Hamiltonian, the quantum fluctuation could further lower the energy, and the amount is dependent on the classical configurations, resulting in the lifting of degeneracy. Starting from the identical classical system, usually the quantum and thermal fluctuations result in similar outcomes and select the same ground state for weakly frustrated magnets. However, this is not always guaranteed, and many counterexamples have been provided [13,16,21,37]. Therefore, it is worthwhile to examine the quantum version of this OBD effect. However, this effect has not yet been studied to the best of our knowledge. One possible reason is because such a system can hardly be prepared in real materials. However, the recent success in simulating various quantum systems with neutral Rydberg atoms [38,39] has attracted huge attention, leading to the so-called quantum simulator [40–43]. It has been shown that the quantum Ising model with both longitudinal and transverse fields can be simulated [44] by utilizing the Rydberg blockade [45,46]. Other spin models, such as the quantum XY model [47–49], XXZ model [50,51], or even the XYZ model [52], can also be generated through microwave engineering. In the following content we will provide a possible setup to study the quantum OBD effect in our target system. We also conduct both analytical and numerical calculations and conclude that the stripe pattern is ultimately selected by the OBD effect. Our conclusion based on the theoretical analysis could become a good benchmark for the real-world device of a two-dimensional quantum simulator using Rydberg atoms in the future.

Moreover, thanks to the advance of cold-atom techniques [53–56], many physical scenarios can now be simulated with emphasized quantum effect, leading to another type of quantum simulators. Especially, dipolar quantum gases made of erbium and dysprosium recently attracted wide attention for the realization of supersolids out of their Bose-Einstein condensates [57–61]. Note that, by placing dipolar molecules in optical lattices, researchers have realized suitable quantum simulators for various Hamiltonians with electric [62–66] or magnetic dipoles [67]. While Rydberg atoms are often used to create the electric dipole-dipole interaction to synthesize the spin exchange interaction, molecules carrying magnetic dipoles can be viewed as a bosonic system probed by the Bose-Hubbard model [68–70]. This makes the related studies of various extended Bose-Hubbard models necessary, and many studies have been done [71–85]. In our previous work, we studied the effect by tilting the polar angle of a dipole and realized a competing scenario between different lattice structures [77]. Within the original square lattice, we discovered that a three-sublattice supersolid phase ought to show up by tilting the polar angle. Related studies have also demonstrated the potential of such techniques in fabricating artificial physical scenarios of interest. Besides the quantum OBD effect by Rydberg-atom simulator, in this work we also study hard-core bosons with dipole-dipole interaction in a triangular lattice with different tilted dipolar angles, mimicking the distortion of the lattice.

In the following content, we will first study the quantum OBD effect using the real space perturbation theory (RSPT) [16,86–90] and infinite projected entangled-pair state (iPEPS)

[91–93]. We first map the two-level Rydberg system to a spin-1/2 scenario and show that when the number of up spins (n_\uparrow) is equal to that of down spins (n_\downarrow), a subextensive degeneracy is present in the classical limit. Introducing the spin exchange coupling, energy correction can be considered with RSPT, and we focus on the leading-order correction between the stripe and kinked configurations. Our calculation shows that the energy correction favors the stripe pattern, coinciding with previous results for thermal OBD [36]. As a further confirmation we apply the iPEPS calculation for a simplified toy model, showing that the stripe state is indeed more stable. Next, for the dipolar bosons in a triangular optical lattice with tilted polar angle we conduct numerical simulations with the cluster mean-field theory (CMFT), which has been shown effective in capturing distinct phases in our previous work [77]. We unveil fruitful phase diagrams with various underlying phases, including the supersolid phase. We then conclude our work and argue some potential scopes for further studies.

II. QUANTUM OBD EFFECT

A. Rydberg-atom quantum simulator

The adoption of Rydberg atoms for a quantum simulator has recently become a topic of interest. It has been shown that the quantum Ising model can be synthesized in a large scale with many interesting properties [94–96], as well as the potential application for quantum information [40]. However, the adoption of Rydberg atoms for quantum simulation or computation is largely hindered by the limited lifetime (a few 100 μs) for low-angular-momentum (ℓ) Rydberg states [97]. In contrast, when exciting the Rydberg states to a very large principal quantum number (n) and utilizing the levels with largest ℓ and magnetic quantum number (m), the lifetimes of these Rydberg states, named circular Rydberg states [98], can be greatly enhanced. Their naturally long lifetime originates from the fact that these large- ℓ states can only decay through the emission of a low-frequency photon, which is polarized parallel to the quantization axis. This feature makes the lifetime of circular Rydberg states much longer than that of regular low- ℓ Rydberg states. Since it is a single-mode decay, the lifetime can be further elongated by placing the atoms in an environment which prohibits the field of resonance of the atomic transition [99,100]. Adopting a capacitor parallel to the plane where atoms reside, the lifetime again gets largely enhanced, and a useful lifetime of at least 1.1 s for an atomic chain has been reported [101]. Such a measure can even be helpful for a non-zero-temperature environment, and a millisecond-lifetime circular Rydberg state was recently reported at room temperature [102]. This makes the quantum simulation and quantum computation much more feasible [101,103,104].

From now on we denote the circular Rydberg states as $|nC\rangle$, and such states fulfill the following condition: $\ell = |m| = n - 1$. These states have a wave function distribution of a torus whose circular orbit has a radius $r_n = a_0 n^{3/2}$, where a_0 is the Bohr radius. The circular states can be stabilized by an external electric field (F), which also defines the quantization axis, perpendicular to the plane of circular orbits. Through a proper measure a two-level system composed of two circular

states, $|n_1C\rangle$ and $|n_2C\rangle$, where $n_2 > n_1$ and C means the circular state, can be generated.

The interaction between any two Rydberg atoms comes from the electric dipoles carried by the atoms themselves, leading to a manifest dipole-dipole interaction [105,106]. When two atoms are far from each other the interaction hardly affects the two-atom Rydberg state and thus a second-order perturbation is adopted, giving rise to a van der Waals interaction proportional to $1/r^6$, where r represents the distance between sites [107,108]. On the other hand, when the energy defect of two dipole-dipole coupled states is tuned to zero the strongest Rydberg-Rydberg interaction, proportional to $1/r^3$, appears through the Förster resonance process [109,110]. According to Ref. [101] one needs to choose $n_2 = n_1 \pm 2$ to have a flexible simulator, where both the spin-exchange and van der Waals interaction are proportional to $1/r^6$. Since the spin-exchange effect might lead to the decay of circular states to nearby degenerate states, a magnetic field (B) parallel to the electric field is cast so that the highly degenerate hydrogenic manifold of the same principal quantum number n can be lifted and the circular state is thus isolated [101]. The magnetic field also prohibits the hybridization of spin up and down channel in each circular state. As a result, we obtain clean two-level Rydberg states for the purpose of quantum simulation.

The Hamiltonian for a pair of Rydberg atoms with the basis $[|n_1C, n_1C\rangle, |n_1C, n_2C\rangle, |n_2C, n_1C\rangle, |n_2C, n_2C\rangle]$ can then be written as [101]

$$H \propto \begin{bmatrix} h_{n_1-n_1} & 0 & 0 & 0 \\ 0 & h_{n_1-n_2} & v_{n_1-n_2} & 0 \\ 0 & v_{n_1-n_2} & h_{n_1-n_2} & 0 \\ 0 & 0 & 0 & h_{n_2-n_2} \end{bmatrix}, \quad (1)$$

where in the Pauli basis it reads

$$H \propto J(\sigma_1^x \sigma_2^x + \sigma_1^y \sigma_2^y) + J_z \sigma_1^z \sigma_2^z - B_z(\sigma_1^z + \sigma_2^z), \quad (2)$$

with

$$\begin{aligned} J &\propto |v_{n_1-n_2}|, \\ J_z &\propto h_{n_1-n_1} + h_{n_2-n_2} - 2h_{n_1-n_2}, \\ B_z &\propto \frac{1}{2}(h_{n_1-n_1} - h_{n_2-n_2}). \end{aligned} \quad (3)$$

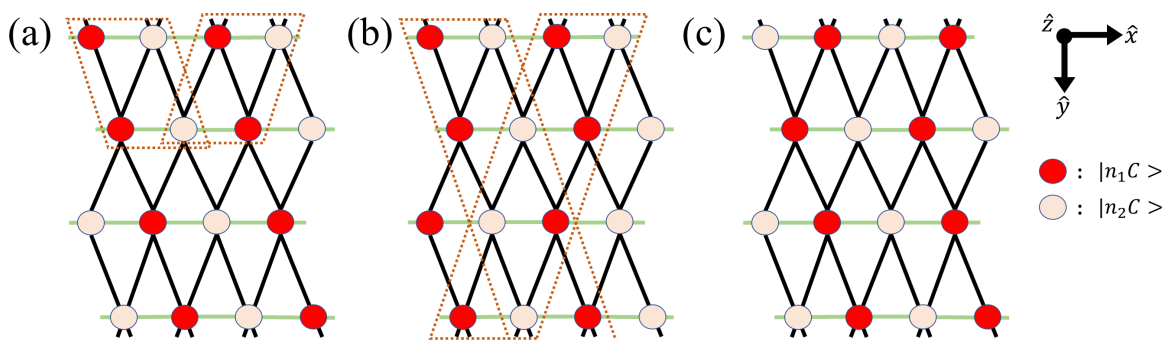


FIG. 1. Configurations for (a) stripe, (b) kinked, and (c) mixed states. Red (pink) dots indicate that the Rydberg atom occupies the $|n_1C\rangle$ ($|n_2C\rangle$) state, and the black (green) bonds represent the bonds for diagonal (horizontal) interaction, written as J_d^z (J_h^z) in Eq. (4) (also see the context). The brown dotted boxes indicate the minimum repeated unit cell for the stripe and kinked patterns, which we will later adopt for the iPEPS calculation.

While J is independent on the magnetic and electric fields, J_z and B_z are susceptible to the field strength; when the intersite spacing is $5 \mu\text{m}$, $h_{48-48} = 2.2 \text{ GHz } \mu\text{m}^6$, $h_{48-50} = 2.66 \text{ GHz } \mu\text{m}^6$, and $h_{50-50} = 3.03 \text{ GHz } \mu\text{m}^6$ as $F = 9 \text{ V/cm}$ and $B = 13 \text{ G}$, while $v_{48-50} = -0.539 \text{ GHz } \mu\text{m}^6$ stays independent of F and B [101].

Placing the circular Rydberg atoms in the optical lattice [111,112], a highly tunable simulator for the effective XXZ model with longitudinal field can thus be formed. In order to engineer the triangular lattice to simulate the quantum OBD effect, a better way is to trap the individual atom using optical tweezers [113]. One recent work has demonstrated such a possibility by trapping rubidium circular Rydberg atoms into a 3×6 array of tweezers [114]. It is reported that the trapping time can scale to over a few milliseconds while the simulation time only demands a few microseconds. A very recent paper reported the existence of long-lived circular Rydberg states by trapping the alkaline-earth atoms using optical tweezers [115]. Their discovery also widens the potential usage of this kind of quantum simulator. Therefore, by properly manipulating the positions of optical tweezers, a deformed triangular optical lattice can be generated, as shown in Fig. 1. There, the diagonal bonds (black bonds) have longer intersite spacing so that the subextensive degeneracy in the classical limit ($J = 0$) can be simulated. We demonstrate three different configurations in Fig. 1, for the (a) stripe, (b) kinked, and (c) mixed configurations. Mixture of stripe and kinked configurations in a larger lattice gives rise to various possible states, forming the manifold degeneracy. Note that the diagonal spacing needs to be large enough to prohibit the off-diagonal magnetic orders.

Since the basic setup has been introduced, next we will discuss the theoretical and numerical tools to study this quantum OBD effect, which can benchmark a real-world device of a two-dimensional quantum simulator with Rydberg atoms.

B. Real space perturbation theory

We first introduce the RSPT and derive the formula in this section. In this work we study the effect of spin-exchange quantum fluctuation on a system of Rydberg atoms, which can be represented as $\sum_{\langle ij \rangle} (\hat{S}_i^+ \hat{S}_j^- + \hat{S}_i^- \hat{S}_j^+)$. As a result, the target Hamiltonian represented by spin-1/2 operators can be

written as

$$H = J \sum_{\langle ij \rangle} (\hat{S}_i^+ \hat{S}_j^- + \hat{S}_i^- \hat{S}_j^+) + \sum_{\langle ij \rangle} J_{ij}^z \hat{S}_i^z \hat{S}_j^z - \sum_i \mathbf{B} \cdot \hat{\mathbf{S}}_i, \quad (4)$$

where $J_{ij}^z \gg |J|, |\mathbf{B}|$ and \mathbf{B} represents the external Zeeman field. We assign J to be isotropic since later we will find out that only the perturbative processes concerning the diagonal spin exchange would matter. To effectively reflect the anisotropy caused by the deformed lattice, we assign J_{ij}^z equal to J_d^z when the bond is in the diagonal direction (black bonds in Fig. 1) and J_h^z when the bond is in the horizontal direction (green bonds in Fig. 1). When $J_d^z < J_h^z$ and $n_\uparrow = n_\downarrow$, the ground state configuration enjoys a manifold degeneracy because the same spins tend to align along the diagonal direction. However, due to the fact that there are two diagonal bonds, we can have many different degenerate configurations and the total number is equal to 2^{L_y-1} , where L_y is the number of rows along \hat{y} direction. As a result, the ground state entropy $S_{\text{GS}} \sim L_y - 1$, leading to a subextensive degeneracy. Among these degenerate configurations there are two special patterns, the stripe and kinked states. The stripe state is composed of parallel straight lines of up and down spins [Fig. 1(a)], while for the kinked state there are three sublattices occupied by up or down spins within each vertical diamond of the triangular lattice [Fig. 1(b)]. The remaining degenerate states, called the mixed states, are simply the combinations of stripe and kinked states in specific proportions [one example is shown in Fig. 1(c)].

To apply RSPT, one needs to rotate the local coordinate on each site so that every spin points along the \hat{z} direction. Thus, we rewrite the corresponding spin-1/2 Hamiltonian in the following form:

$$H = \sum_{\langle ij \rangle} \mathbf{S}_i \cdot \mathbf{J} \cdot \mathbf{S}_j - \sum_i \mathbf{B} \cdot \mathbf{S}_i, \quad (5)$$

with

$$\mathbf{J} = \begin{cases} \text{diag}(2J, 2J, J_d^z) & \text{if } \langle ij \rangle \parallel \text{horizontal direction,} \\ \text{diag}(2J, 2J, J_h^z) & \text{if } \langle ij \rangle \parallel \text{diagonal direction.} \end{cases} \quad (6)$$

We can extend this to a more generalized Hamiltonian with longer-range hopping or even off-diagonal terms if needed, simply by modifying the form of coupling matrices. In Eq. (5), $\mathbf{S}_i = S_i^+ \hat{e}_i^- + S_i^- \hat{e}_i^+ + S_i^z \hat{e}_i^z$ with $\hat{e}_i^\pm = \frac{1}{2}(\hat{e}_i^\pm \pm i\hat{e}_i^y)$ and the classical configuration on each site is $\mathbf{S}_i^{(0)} = S \hat{e}_i^z$. Note that now S^\pm and S^z are no longer operators. They simply represent the corresponding operation for the classical spin. Our choice of the ‘‘unit’’ vectors guarantees the transformation to be unitary, although its length is not necessarily unity. This also explains why we have a prefactor of 2 for J in Eq. (6). Next, we expand the equation and the result becomes

$$\begin{aligned} H = & \sum_{\langle ij \rangle} (\hat{e}_i^+ \cdot \mathbf{J} \cdot \hat{e}_j^+ S_i^- S_j^- + \text{H.c.}) \\ & + (\hat{e}_i^+ \cdot \mathbf{J} \cdot \hat{e}_j^- S_i^- S_j^+ + \text{H.c.}) \\ & + (\hat{e}_i^+ \cdot \mathbf{J} \cdot \hat{e}_j^z S_i^- S_j^z + \hat{e}_i^- \cdot \mathbf{J} \cdot \hat{e}_j^z S_i^+ S_j^z + \text{H.c.}) \\ & + \hat{e}_i^z \cdot \mathbf{J} \cdot \hat{e}_j^z S_i^z S_j^z \\ & - \sum_i \mathbf{B} \cdot \hat{e}_i^- S_i^+ + \mathbf{B} \cdot \hat{e}_i^+ S_i^- + \mathbf{B} \cdot \hat{e}_i^z S_i^z. \end{aligned} \quad (7)$$

After introducing the quantum fluctuation, the spin configuration does no longer align along the local \hat{e}_i^z direction and thus we can replace S_i^z by $S - \delta S_i$. Then, Eq. (7) becomes

$$H = H_0 + H_{\text{unperturbed}} + H_p, \quad (8)$$

where

$$H_0 = S^2 \sum_{\langle ij \rangle} \hat{e}_i^z \cdot \mathbf{J} \cdot \hat{e}_j^z - S \sum_i \mathbf{B} \cdot \hat{e}_i^z, \quad (9)$$

representing the classical energy. And $H_{\text{unperturbed}}$ is

$$\begin{aligned} H_{\text{unperturbed}} = & -S \sum_{\langle ij \rangle} \hat{e}_i^z \cdot \mathbf{J} \cdot \hat{e}_j^z (\delta S_i + \delta S_j) \\ & + \sum_{\langle ij \rangle} \hat{e}_i^z \cdot \mathbf{J} \cdot \hat{e}_j^z \delta S_i \delta S_j + \sum_i \mathbf{B} \cdot \hat{e}_i^z \delta S_i. \end{aligned} \quad (10)$$

Since Eq. (10) does not change the spin configuration, it will not contribute to the perturbation. At last, the perturbative Hamiltonian H_p is written as

$$H_p = \sum_{\langle ij \rangle} (J_{ij}^{(1)} + J_{ij}^{(2)} + J_{ij}^{(3)}) - \sum_i B_i, \quad (11)$$

where

$$\begin{aligned} J_{ij}^{(1)} &= \hat{e}_i^+ \cdot \mathbf{J} \cdot \hat{e}_j^+ S_i^- S_j^- + \text{H.c.}, \\ J_{ij}^{(2)} &= \hat{e}_i^+ \cdot \mathbf{J} \cdot \hat{e}_j^- S_i^- S_j^+ + \text{H.c.}, \\ J_{ij}^{(3)} &= \hat{e}_i^+ \cdot \mathbf{J} \cdot \hat{e}_j^z S_i^- S_j^z + \hat{e}_i^- \cdot \mathbf{J} \cdot \hat{e}_j^z S_i^+ S_j^z + \text{H.c.}, \\ B_i &= \mathbf{B} \cdot \hat{e}_i^- S_i^+ + \mathbf{B} \cdot \hat{e}_i^+ S_i^-. \end{aligned} \quad (12)$$

With these transverse perturbative terms, we can evaluate the energy correction with H_p in n th order with

$$\delta E^{(n)} = \sum_{\{\psi_i\}} \frac{\langle 0 | H_p | \psi_1 \rangle \langle \psi_1 | H_p | \psi_2 \rangle \cdots \langle \psi_{n-1} | H_p | 0 \rangle}{(E_0 - E_{\psi_1}) \cdots (E_0 - E_{\psi_{n-1}})}, \quad (13)$$

where E_0 is the energy for the classical configuration, $|0\rangle$, and E_{ψ_i} is the energy for intermediate state denoted by $|\psi_i\rangle$. The summation will run over every possible intermediate processes for a given order. For any order of perturbation, its energy correction is obtained under several rules:

(1) Each perturbation is evaluated within a linked cluster to ensure the extensiveness of energy correction. On each bond of such a cluster H_p can be applied more than one time, and the total number of executions of H_p determines the order of perturbation.

(2) Any series must start and end with $J_{ij}^{(1)}$ and $J_{ij}^{(3)}$, since we have rotated the local coordinate so that, for every site, $\mathbf{S}_i^{(0)} = S \hat{e}_i^z$.

(3) $J_{ij}^{(3)}$ and B_i only consider one spin flip and thus there must be an even number for such process in a series. Because of this constraint, one can always find a lower order series without these two terms, and therefore we can ignore them in search of leading-order correction.

Because of the above rules, we know that effective leading-order perturbative series must start and end with $J_{ij}^{(1)}$ and are composed of $J_{ij}^{(1)}$ and $J_{ij}^{(2)}$. In Eq. (13), the denominator considers the energy difference between classical and

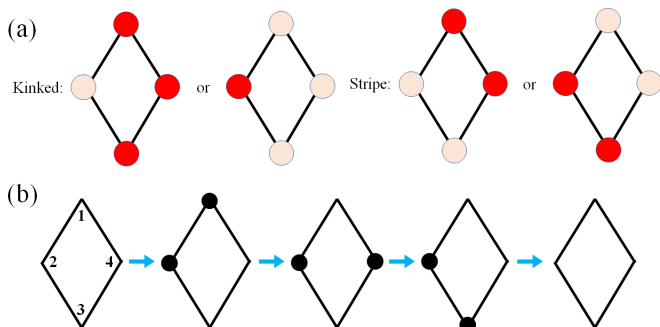


FIG. 2. (a) The four-site diamond cluster that distinguishes kinked and stripe states. Red and pink dots indicate sublattice a and b separately. For the kinked state it has two configurations with three sublattices a or b , while for the stripe state the numbers of a and b sublattice are equal. (b) An example of the fourth-order tunneling process within the diamond cluster. The perturbative process corresponds to $J_{12}^{(1)} \rightarrow J_{14}^{(2)} \rightarrow J_{34}^{(2)} \rightarrow J_{23}^{(1)}$. Black dots indicate the places where spins have been flipped.

intermediate configurations. It is given by

$$E_0 - E_\psi = \langle 0|H|0\rangle - \langle \psi|H|\psi\rangle = -\langle \psi|H_{\text{unperturbed}}|\psi\rangle. \quad (14)$$

To adopt RSPT, first we rotate the local coordinates so that $\mathbf{S}_i^{(0)} = S\hat{e}_i^z$. Our classical configurations are composed of two different sublattices representing the up and down spins,

$$\hat{e}_a^z = (\sin \phi_a, 0, \cos \phi_a), \quad \hat{e}_b^z = (\sin \phi_b, 0, \cos \phi_b), \quad (15)$$

and then we choose

$$\begin{aligned} \hat{e}_a^\pm &= \frac{1}{2}(\cos \phi_a, \pm i, -\sin \phi_a), \\ \hat{e}_b^\pm &= \frac{1}{2}(\cos \phi_b, \pm i, -\sin \phi_b), \end{aligned} \quad (16)$$

where a and b denote two different sublattices. Without loss of generality, we choose the planar spin orienting along the \hat{x} axis. In fact, in the classical limit we can simply assign $\phi_a = 0$ for up spin and $\phi_b = \pi$ for down spin. Since we hope that our derivation can also be useful in the more general scenarios breaking the $U(1)$ symmetry, we take the off-diagonal order into our consideration. It is also clear to see that by adopting the same coordinate of sublattice a or b for every site in Eq. (7), we can resume the original Hamiltonian, Eq. (4), where the translation invariance is accompanied.

To estimate the leading-order correction, we need to first look for the minimal closed cluster which differentiates the stripe and kinked patterns, and it is the vertical diamonds whose longer diagonal line is parallel to \hat{y} in Fig. 1. In Fig. 2(a) we demonstrate the minimal different cluster for kinked and stripe states. Then, we need to flip the spins through the intermediate process on the diamond bonds to evaluate the energy correction. Since there are four bonds on each diamond, the leading-order correction which we are looking for is of the fourth order. One of the possible intermediate processes is shown in Fig. 2(b).

The detailed equations and derivation of RSPT are shown in Appendix A, and here we only demonstrate the final results. While the degeneracy stays intact when $J = 0$, turning on the

spin-flip coupling will immediately introduce an energy correction to different patterns. For the stripe and kinked patterns, we have $\phi_a = 0$ and $\phi_b = \pi$ for the classical configurations. Under this assumption our equations can be largely simplified. More importantly, $J_3^{d(2)}$ becomes zero and thus only a few terms remain in Eqs. (A4) and (A5). The energy correction terms then become

$$\begin{aligned} \delta E_{\text{kinked}}^{(4)} &= \frac{2J^4}{(\Gamma_3)^2\Gamma_4}, \\ \delta E_{\text{stripe}}^{(4)} &= \frac{2J^4}{(\Gamma_3)^2\Gamma_4} + \frac{2J^4}{(\Gamma_3)^2\Gamma_5}. \end{aligned} \quad (17)$$

Since J_h^z is repulsive and thus $\Gamma_5 = -8S^2J_h^z < 0$ (see Appendix A), the stripe configuration is favored and would be selected. This conclusion coincides with the previous one for the frustrated colloidal soft matter system, whose thermal OBD has been studied through the entropy estimation [36]. There, the authors have shown that the straight stripe configuration possesses lower free energy, despite the fact that during the cooling process the energy barrier among different configurations will eventually lead to a mixed pattern. The effective Hamiltonian of such a system can be written down as an antiferromagnetic Ising model with deformation in the triangular lattice, similar to our system considered here. Last, we emphasize that, since the leading-order correction is of the fourth order, the sign of J does not affect the final conclusion. In Sec. III, we will consider an effective model with the ferromagnetic J .

C. iPEPS calculation

Since RSPT applies well only for small J , we would like to see if the conclusion still holds when the quantum fluctuation is strong. For this purpose, we adopt a two-dimensional (2D) tensor network ansatz, the infinite projected entangled-pair state (iPEPS), to numerically calculate the simplified Eq. (4),

$$H_s = J \sum_{\langle ij \rangle} (\hat{S}_i^+ \hat{S}_j^- + \hat{S}_i^- \hat{S}_j^+) + J^z \sum_{\langle ij \rangle \in h} \hat{S}_i^z \hat{S}_j^z, \quad (18)$$

where we consider the extreme case and ignore both the Ising coupling along the diagonal direction and the longitudinal field. By properly choosing the pre-designated unit-cell size (in this work 2×2 or 4×2 as shown in Fig. 1) and optimizing the $d \times D \times D \times D \times D$ tensors, where d represents the dimension of local Hilbert space and D is the virtual bond dimension, this tensor network ansatz serves as a good variational wave function for quantum many-body systems. We provide some details of iPEPS in Appendix B.

To numerically estimate the ground state ansatz of Eq. (18), we need to adopt numerous trials starting from different initial setups. Because we already recognize that there are many competing states (stripe, kinked, or mixed states), we need to avoid the simulation being trapped in some undesirable local minima. As a result, besides the random initial tensors we also start our calculation by constructing the distinct product states, corresponding to the stripe and kinked configurations separately. Since the product state is of $D = 1$, we then enlarge our tensors to the assigned D , with extra tensor elements being small random numbers. Through this measure, we guide the

TABLE I. We provide the values of energies and orders for several J/J_z , with bond dimension $D = 2$ or 3.

J/J_z	$D = 2$				$D = 3$			
	$\langle H_s \rangle$	m	\tilde{S}^z	\tilde{S}^+	$\langle H_s \rangle$	m	\tilde{S}^z	\tilde{S}^+
0.1	-0.26327	0.47966	0.47966	0.00002	-0.26336	0.47880	0.47880	0.00004
0.2	-0.29746	0.43363	0.43363	0.00004	-0.29843	0.42404	0.42404	0.00007
0.3	-0.34539	0.38197	0.38197	0.00004	-0.34853	0.35545	0.35545	0.00032
0.4	-0.40150	0.33782	0.33782	0.00007	-0.40753	0.29673	0.29673	0.00108
0.5	-0.46177	0.30808	0.30808	0.00001	-0.47140	0.25309	0.25308	0.00174
0.6	-0.52501	0.28392	0.28392	0.00003	-0.53779	0.22126	0.22122	0.00372
0.7	-0.58987	0.26586	0.26586	0.00005	-0.60623	0.18589	0.18586	0.00359

optimization toward obtaining the stripe or kinked state. After the convergence is reached, the averaged magnetization is defined as

$$m = \frac{1}{N_C} \sum_{i \in C} \sqrt{\langle \hat{S}_i^x \rangle^2 + \langle \hat{S}_i^y \rangle^2 + \langle \hat{S}_i^z \rangle^2}, \quad (19)$$

where C means the repeating unit cell and N_C is the number of lattice sites within the cell. For the stripe pattern, since there are two possible choices for the iPEPS unit cell and they correspond to the wave numbers $(0, \pi)$ and (π, π) after Fourier transformation, we thus define the two related orders for the stripe pattern. The first one is the diagonal magnetic moment

$$\tilde{S}^z = \frac{1}{N_C} \sum_{i \in C} \sum_{\mathbf{k} \in \mathbf{k}_1, \mathbf{k}_2} \langle \hat{S}_i^z \rangle e^{i\mathbf{k} \cdot \mathbf{r}_i}, \quad (20)$$

where $\mathbf{k}_1 = (\pi, \pi)$ and $\mathbf{k}_2 = (0, \pi)$. \mathbf{r}_i represents the coordinate (r_i^x, r_i^y) for each site within the unit cell. For the off-diagonal order, we define

$$\tilde{S}^+ = \frac{1}{N_C} \sum_{i \in C} |\langle \hat{S}_i^+ \rangle|. \quad (21)$$

In Table I we provide the lowest energies as well as the orders for several different J . We can clearly see that for each J/J_z we have $m \approx \tilde{S}^z$, meaning that despite the different initial trials the states of lowest energy always belong to the stripe state. Although the off-diagonal orders are almost zero, $\langle \hat{S}^z \rangle$ is highly suppressed due to the quantum effect, suggesting that the initial setup for RSPT might not be well applicable. However, our simulation indicates that the conclusion does not change and the stripe state keeps being the ground state, selected by the quantum OBD effect. It is also worth mentioning that for $D = 3$ and $J > 0.3$ no matter what initial states we adopt the ground state ansatz always evolves toward the stripe state. We then conclude that our system, where the circular Rydberg atoms are placed in a deformed triangular optical lattice, favors the existence of the stripe state.

III. DIPOLAR HARD-CORE BOSONS

In the previous section we revealed the quantum OBD effect for the targeted Rydberg system and identified that the stripe state is more stable. Next, we aim to unveil the possible underlying phases for the artificial Hamiltonian of dipolar bosons in the triangular optical lattice, which can be generated with cold-atom simulators. The realization of placing

magnetic cold atoms in optical lattices has been reported for erbium [67] and ytterbium [116], where a three-dimensional (3D) optical lattice is generated with two horizontal lasers in the x - y plane and one vertical laser reflecting the direction of gravity. Confining the atoms in a 3D lattice would help elongate the lifetime by preventing the inelastic collision of atoms [117,118]. The vertical tunneling can be reduced by adopting a laser with a longer wavelength, and thus a quasi-2D system can be synthesized. Reference [67] provides a good example using a laser with wavelength $(\lambda_x, \lambda_y, \lambda_z) = (532, 532, 1064)$ nm, creating an effective 3D optical lattice with size $(l_x, l_y, l_z) = (266, 266, 532)$ nm and a trapping potential $V(x, y, z) = V_x \cos^2(k_x x) + V_y \cos^2(k_y y) + V_z \cos^2(k_z z)$ where V_i is the lattice depth and k_i is the wave vector in a different direction. After preparing the Bose-Einstein condensate (BEC) of the target atoms through an optical dipole trap (ODT), the BEC cloud is then adiabatically loaded to the optical lattice within a timescale of milliseconds. In the end we obtain a long-lived system whose lifetime scales up to a second [67,117]. Our system, however, demands a triangular optical lattice for its realization, and Ref. [30] has unveiled this possibility using Rb BEC. There, they adopt a three-laser trapping within the x - y plane whose wave vectors mutually share a 120° enclosing angle. Optionally, the recent proposal of using optical tweezers to trap cold atoms might also provide a more flexible platform for designing quantum simulators [119,120].

Next we discuss the Hamiltonian of interest and its realization through cold-atom simulators. The magnetic quantum gas is composed of atoms which can be seen as magnetic dipoles even at zero magnetic field. The origin of dipole moment comes from the spin and orbital angular momentum of electrons, as well as some minor contribution from the nuclear spin. This fact results in the high susceptibility of atoms to an external Zeeman field, which we could use to control the overall orientation, expressed by the polar and azimuthal angles shown in Fig. 3, of the magnetic dipoles [68]. This simplifies the general form of dipole-dipole interaction in Ref. [121] and makes it of the following form:

$$V_{ij} = \frac{V}{r_{ij}^3} (1 - 3 \cos^2 \alpha_{ij}), \quad (22)$$

where V is the interactive strength and $r_{ij} = |\vec{r}_i - \vec{r}_j|$. α_{ij} is the included angle by the dipole moment and \vec{r}_{ij} . This interaction contributes to the on-site repulsive interaction, intersite interaction, and the density induced tunneling. In this

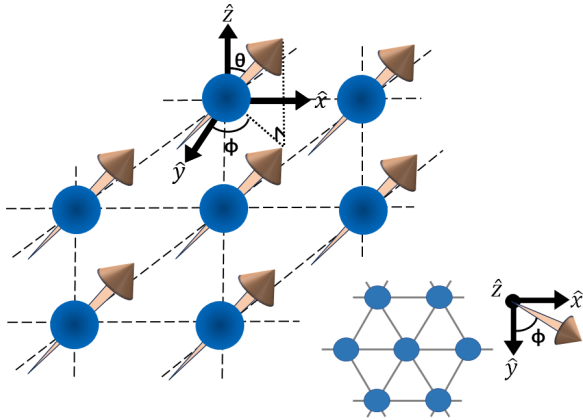


FIG. 3. Schematic demonstration of dipolar interaction in the triangular lattice. Dots denote the lattice site and arrows represent the dipole polarization. Such polarization can be parametrized with polar (θ) and azimuthal (ϕ) angles. The lower right panel shows the projection of the lattice from above for a better demonstration of the azimuthal angle.

work we consider the hardcore limit, meaning that only one atom is allowed to occupy one site in every snapshot. This condition can be naturally fulfilled once the on-site interaction is much larger than the intersite interaction, which can be tuned through controlling the lattice spacing [122]. Once the doubly occupancy is prohibited, the density induced tunneling process also disappears. Along with the normal tunneling process, we end up obtaining the following extended Bose-Hubbard Hamiltonian with the dipolar interaction:

$$H = -t \sum_{\langle ij \rangle} (\hat{b}_i^\dagger \hat{b}_j + \text{H.c.}) + \sum_{\langle ij \rangle} V_{nn} \hat{n}_i \hat{n}_j - \mu \sum_i \hat{n}_i, \quad (23)$$

where \hat{b}_i^\dagger and \hat{b}_i represent the creation and annihilation operators of the hard-core boson, with the number operator being $\hat{n}_i = \hat{b}_i^\dagger \hat{b}_i$. V_{nn} denotes the nn dipole-dipole interaction among bosons and we neglect its long-range tail since it decays rapidly. We emphasize that the dipole-dipole interaction in this section is different from that for the Rydberg atoms. As explained in Sec. II A, for the circular Rydberg atoms one makes use of the electric dipole-dipole interaction of neutral atoms to generate the spin exchange coupling. On the other hand, in this section the cold atom itself can be seen as a magnetic dipole and thus mutual interaction with the form indicated in Eq. (22) is cast among atoms. Moreover, the atoms act as quanta and thus the tunneling effect takes place, minimizing the energy, leading to the hopping term in Eq. (23) that lowers the energy.

The interaction in Eq. (22) can be easily tilted with an external magnetic field. In this work we study the case when the dipole moments are tilted as $\phi = 0$ (see Fig. 3). Thus, for the nn interaction, the two interactive terms along diagonal direction are equal and become attractive when polar angle θ is large enough. Therefore, there are two different terms for V_{nn} :

$$\begin{aligned} V_{nn}^h &= V, \\ V_{nn}^d &= V(1 - \frac{9}{4} \sin^2 \theta), \end{aligned} \quad (24)$$

where indices h and d indicate the interaction along the horizontal and diagonal directions, as shown in Fig. 1, labeled by green and black bonds. As a result, Eq. (23) is akin to Eq. (4) with negative J since there is a one-to-one mapping by simply replacing $\hat{b}_i^\dagger \rightarrow \hat{S}_i^+$, $\hat{b}_i \rightarrow \hat{S}_i^-$, and $\hat{n}_i \rightarrow \hat{S}_i^z + \frac{1}{2}$ [26]. Therefore, by numerically studying Eq. (23) with different tilting angles, the resulting phase diagrams cover a wide range of XXZ-like models with anisotropy in the triangular lattice.

In this work, we adopt CMFT [73,74,77] for the construction of phase diagram. Some details of applying CMFT are indicated in Appendix C. When the strength of the hopping term is small, the ground state is an ordered state with $U(1)$ symmetry preserved. As we increase t , the solid order will dissolve and the phase transits to the superfluid state through a first-order phase transition. However, in some small windows between solid and superfluid phases, two orders, namely the structural and superfluid orders, can coexist and a supersolid phase manifests. To identify distinct phases we first introduce the order parameters adopted here. Solid and supersolid phases both possess structural order which is defined as

$$\tilde{n}(\mathbf{k}) = \frac{1}{N_C} \sum_{i \in C} \langle \hat{n}_i \rangle e^{i\mathbf{k} \cdot \mathbf{r}_i}, \quad (25)$$

where C again represents the repeating unit cell whose size is equal to 3×3 or 4×4 in our CMFT calculation, and thus $N_C = 9$ or 16 . As for the superfluid order, we calculate its condensate density defined as

$$\rho_0 = \frac{1}{N_C} \sum_{i \in C} |\langle \hat{b}_i \rangle|^2. \quad (26)$$

The above two order parameters help identify different phases in our numerical phase diagrams.

We then conduct the CMFT calculation and plot the phase diagrams for several polar angles in Fig. 4. When tilting is small [Fig. 4(a)], the diagonal solid (blue) and supersolid (purple) dominate the phase diagram before entering the superfluid phase. Its structural factor has the modulating momentum $(2\pi/3, 2\pi/3)$, and is named after the diagonal stripe in our earlier work [77]. In the supersolid phase the $\tilde{n}(2\pi/3, 2\pi/3)$ and ρ_0 orders coexist. This phase appears after a continuous transition from the diagonal solid. Further enlarging t , solid order disappears and the phase transits into superfluid (red) phase discontinuously.

On the other hand, the central orange lobe indicates the classically highly degenerate solid configurations (stripe, kinked, and mixed). Thanks to the diagnosis of RSPT and iPEPS in the previous section, we have learned that the true ground state must be in the stripe configuration, although the numerical energies of stripe and kinked configurations by CMFT are very close to each other due to the small t . The green phase in Figs. 4(b) and 4(c) represents a supersolid phase coming from the stripe solid and thus we call it the stripe supersolid. Note that our results indicate that the transition from stripe solid to stripe supersolid, as well as the one from stripe supersolid to superfluid, are both continuous.

One can see from Fig. 4 that as we further tilt the polar angle, the central lobe grows and its corresponding supersolid phase also starts to appear [Fig. 4(b)]. Finally, as the polar angle is large enough, dominant ordered phases in the phase

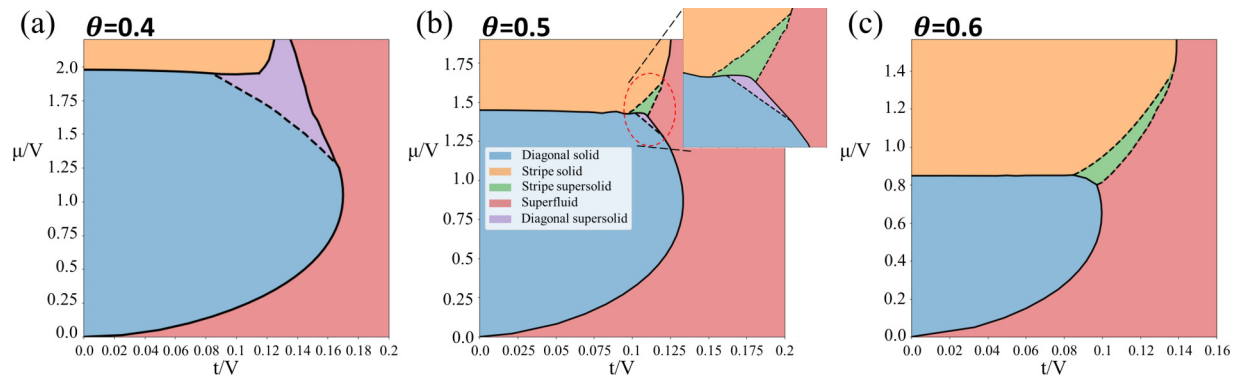


FIG. 4. CMFT phase diagrams with nn dipolar interaction with polar angle equal to (a) 0.4, (b) 0.5, and (c) 0.6, which approximate to 0.127π , 0.159π , and 0.191π . The inset in (b) enlarges the area for two supersolid phases. Solid (dashed) phase boundaries indicate the first-order (second-order) phase transition.

diagram will be replaced by the stripe solid and supersolid [Fig. 4(c)]. The scenario described here is just opposite to the one in our previous work, where a square lattice effectively shifts to a triangular one by tilting the polar angle [77]. Here, we start from the triangular lattice where the corresponding phase possesses three sublattices (see, e.g., Fig. 3 in Ref. [77] for explanation), and eventually ends up with a square one with only two sublattices, according to the phase diagram. Last, we emphasize that including the long-range tail of dipole-dipole interaction will automatically lift the degeneracy even in the classical limit. In such a scenario we expect an even more fruitful phase diagram with many different ground-state configurations, but it requires a highly precise experimental tool to sort out. We will leave the further studies of this issue for future work.

IV. CONCLUSION

In this work we study two different systems of a dipolar quantum simulator. Placing circular Rydberg atoms in a deformed triangular optical lattice, a subextensive degeneracy can be realized and the spin exchange interaction, arising from the electric dipole-dipole interaction of Rydberg atoms leads to the quantum OBD effect. The degeneracy of lowest-energy configuration in the classical limit is caused by deformation, making the van der Waals repulsion only be seen in the horizontal direction between nearby sites. Once the spin exchange term is introduced, the overall Hamiltonian is akin to the XXZ model with anisotropic interactive potential. With RSPT and iPEPS, we predict that the stripe configuration is the true ground state, in coincidence with the thermal counterpart of this OBD effect according to the previous work [36]. Next, we consider an extended Bose-Hubbard model with magnetic dipole-dipole interaction in an optical lattice, which is related to the cold-atom quantum simulator. We then provide the phase diagrams for the nn dipolar hard-core bosonic Hamiltonian with different tilting angles in the triangular lattice, using CMFT. We exploit the competing scenario proposed in our earlier work [77] and demonstrate that the effective lattice structure shifts from triangular lattice to a square one, as well as various different phases including the supersolid.

The technique of neutral atoms for quantum computing has recently attracted huge attention. By placing the Rydberg atoms with the desirable geometric controls, large-scale quantum Hamiltonian can be simulated with quantum analog simulators [123]. However, the current platforms mainly focus on the Ising model and its variants. In this work, we push one step forward and combine the spin exchange interaction as well as the van der Waal repulsion. We propose a possible experimental setup using the circular Rydberg atoms in an optical lattice for realization, which benefits further investigation by experimental groups. Our analytical and numerical studies, as well as the conclusion, might be useful benchmarks once the simulator can be put into practice, instead of checking the full phase diagram (see, e.g., Sec. III B of Ref. [101]). Moreover, controlling the anisotropy of the triangular lattice, we might reach a novel regime where the order disappears and a state with larger entanglement entropy manifests [44]. This would benefit further studies with quantum simulators as well as numerical calculation through quantum Monte Carlo or tensor networks, and we will leave it for future consideration. It is also important to note that our proposal unveils a possible protocol for studying the dynamics of glassy phases through a quantum simulator. In Ref. [36] the authors revealed that although the straight stripe benefits from lower free energy and should be more favorable in the arbitrarily low temperature region, the free-energy barrier between different configurations results in a metastable disorder state while cooling down the temperature. Similarly, if we introduce the spin exchange coupling in the same manner a nontrivial glassy dynamics [124] can likely be simulated.

Moreover, a quantum simulator made of cold atoms with magnetic dipoles plays another important role in simulating the extended Bose-Hubbard model. While each atom can be seen as a magnetic dipole, their collective alignment can be manipulated by an external field. By tilting the polar angle of dipoles, the corresponding phase diagram changes and peculiar phases also appear. This implies that through some simple action, such as tilting the polar angle, many extraordinary physical scenario can be artificially realized through such quantum simulators. In sum, we believe that our proposals both indicate alternative paths in applying quantum simulators for studying intriguing physics and demonstrate their great potential for artificial many-body systems.

ACKNOWLEDGEMENTS

W.-L.T. acknowledge the useful discussions with Mike Zhitomirsky during the International Conference on Strongly Correlated Electron Systems 2023 (SCES 2023), with Pedro Lopes from QuEra Computing Inc., with Thomas Ayrar during the SQAI-NCTS Workshop on Tensor Network and Quantum Embedding in Tokyo, and with Hyun-Yong Lee, Tsuyoshi Okubo, S. R. Ghazanfari, and Xinliang Lyu. The authors also acknowledge the Advanced Study Group (ASG) Tensor Network Approaches to Many-Body Systems organized by the Center for Theoretical Physics of Complex Systems (PCS) of the Institute for Basic Science (IBS) in Daejeon, Korea. H.-K.W. is supported by JQI-NSF-PFC (supported by NSF Grant No. PHY-1607611). N.K. is supported by Japan Society for the Promotion of Science (JSPS) KAKENHI Grants No. JP19H01809 and No. JP23H01092. T.S. is supported by JSPS KAKENHI Grant. No. 21K03390. W.-L.T. is supported by the Center of Innovations for Sustainable Quantum AI (Japan Science and Technology Agency (JST) Grant No. JPMJPF2221). This work is also mainly supported by the above-mentioned JST Grant.

APPENDIX A: DETAILS FOR THE REAL SPACE PERTURBATION THEORY

In this Appendix, we work on the details for RSPT. With the choice for the local coordinate shown in the main text [Eqs. (15) and (16)], we can now write down the corresponding $J_{ij}^{(1)}$ and $J_{ij}^{(2)}$ terms. For diagonal bonds we have

$$\begin{aligned} J_{aa}^{d(1)} &= \frac{1}{4} \sin^2 \phi_a (J_d^z - 2J) S_a^+ S_a^+ + \text{H.c.}, \\ J_{bb}^{d(1)} &= \frac{1}{4} \sin^2 \phi_b (J_d^z - 2J) S_b^+ S_b^+ + \text{H.c.}, \\ J_{ab}^{d(1)} &= \frac{1}{4} [2J(\cos \phi_a \cos \phi_b - 1) + J_d^z \sin \phi_a \sin \phi_b] S_a^+ S_b^+ \\ &\quad + \text{H.c.}, \end{aligned} \quad (\text{A1})$$

where we assign $J_1^{d(1)} = \frac{1}{4} \sin^2 \phi_a (J_d^z - 2J)$, $J_2^{d(1)} = \frac{1}{4} \sin^2 \phi_b (J_d^z - 2J)$, and $J_3^{d(1)} = \frac{1}{4} [2J(\cos \phi_a \cos \phi_b - 1) +$

$J_d^z \sin \phi_a \sin \phi_b]$. And

$$\begin{aligned} J_{aa}^{d(2)} &= \frac{1}{4} [2J(1 + \cos^2 \phi_a) + J_d^z \sin^2 \phi_a] S_a^+ S_a^- + \text{H.c.}, \\ J_{bb}^{d(2)} &= \frac{1}{4} [2J(1 + \cos^2 \phi_b) + J_d^z \sin^2 \phi_b] S_b^+ S_b^- + \text{H.c.}, \\ J_{ab}^{d(2)} &= \frac{1}{4} [2J(1 + \cos \phi_a \cos \phi_b) + J_d^z \sin \phi_a \sin \phi_b] S_a^+ S_b^- \\ &\quad + \text{H.c.}, \end{aligned} \quad (\text{A2})$$

where we again set $J_1^{d(2)} = \frac{1}{4} [2J(1 + \cos^2 \phi_a) + J_d^z \sin^2 \phi_a]$, $J_2^{d(2)} = \frac{1}{4} [2J(1 + \cos^2 \phi_b) + J_d^z \sin^2 \phi_b]$, and $J_3^{d(2)} = \frac{1}{4} [2J(1 + \cos \phi_a \cos \phi_b) + J_d^z \sin \phi_a \sin \phi_b]$. For the horizontal bonds we simply need to replace J_d^z in Eqs. (A1) and (A2) with J_h^z , but in fact it does not affect the leading-order correction since our cluster of interest is the vertical diamond [Fig. 2(a)]. Moreover, all possible intermediate configurations as well as their corresponding $-\langle \psi | H_{\text{unperturbed}} | \psi \rangle$, labeled by different Γ and composing the denominator of energy correction, also need to be considered. For this purpose, we first list all the possible intermediate configurations during the spin flipping process, shown in Fig. 5, with each configuration's corresponding minus unperturbed energy, $E_0 - E_\psi$, labeled by different Γ . We list their formulas in Table II. Note that $\Gamma'_k(\textcircled{2}) = \Gamma_k(\textcircled{2})$, $\Gamma'_k(\textcircled{3}) = \Gamma_k(\textcircled{3})$, and $\Gamma'_s(\textcircled{1}) = \Gamma_s(\textcircled{2})$, $\Gamma'_s(\textcircled{2}) = \Gamma_s(\textcircled{1})$, $\Gamma'_s(\textcircled{3}) = \Gamma_s(\textcircled{3})$, $\Gamma'_s(\textcircled{4}) = \Gamma_s(\textcircled{4})$, $\Gamma'_s(\textcircled{5}) = \Gamma_s(\textcircled{5})$. For simplicity, we further conclude that

$$\begin{aligned} \Gamma_1 &= \Gamma_k(\textcircled{1}) = \Gamma_s(\textcircled{2}) = \Gamma'_s(\textcircled{1}), \\ \Gamma_2 &= \Gamma'_k(\textcircled{1}) = \Gamma_s(\textcircled{1}) = \Gamma'_s(\textcircled{2}), \\ \Gamma_3 &= \Gamma_k(\textcircled{3}) = \Gamma'_k(\textcircled{3}) = \Gamma_s(\textcircled{3}) = \Gamma'_s(\textcircled{3}), \\ \Gamma_4 &= \Gamma_k(\textcircled{2}) = \Gamma'_k(\textcircled{2}) = \Gamma_s(\textcircled{4}) = \Gamma'_s(\textcircled{4}), \\ \Gamma_5 &= \Gamma_s(\textcircled{5}) = \Gamma'_s(\textcircled{5}). \end{aligned} \quad (\text{A3})$$

Along with $\Gamma_k(\textcircled{4})$ and $\Gamma'_k(\textcircled{4})$, we have obtained all the ingredients needed for the denominators of the energy corrections.

TABLE II. Different Γ 's for the kinked and stripe configurations. $E_{\mathbf{B}}^a = 2\mathbf{SB} \cdot \hat{e}_a^z$ and $E_{\mathbf{B}}^b = 2\mathbf{SB} \cdot \hat{e}_b^z$. $\Gamma_a = J_d^z \cos^2 \phi_a + 2J \sin^2 \phi_a$ and $\Gamma_b = J_d^z \cos^2 \phi_b + 2J \sin^2 \phi_b$.

Kinked	
$\Gamma_k(\textcircled{1})$	$4S^2 \Gamma_a + 8S^2 (J_d^z + J_h^z) \cos \phi_a \cos \phi_b + 32S^2 J \sin \phi_a \sin \phi_b - 2E_{\mathbf{B}}^a$
$\Gamma_k(\textcircled{2})$	$4S^2 (\Gamma_a + \Gamma_b) + 4S^2 (2J_d^z + J_h^z) \cos \phi_a \cos \phi_b + 24S^2 J \sin \phi_a \sin \phi_b - E_{\mathbf{B}}^a - E_{\mathbf{B}}^b$
$\Gamma_k(\textcircled{3})$	$4S^2 (\Gamma_a + \Gamma_b) + 4S^2 (J_d^z + 2J_h^z) \cos \phi_a \cos \phi_b + 24S^2 J \sin \phi_a \sin \phi_b - E_{\mathbf{B}}^a - E_{\mathbf{B}}^b$
$\Gamma_k(\textcircled{4})$	$8S^2 \Gamma_a + 8S^2 (J_d^z + J_h^z) \cos \phi_a \cos \phi_b + 32S^2 J \sin \phi_a \sin \phi_b - 2E_{\mathbf{B}}^a$
$\Gamma'_k(\textcircled{1})$	$4S^2 \Gamma_b + 8S^2 (J_d^z + J_h^z) \cos \phi_a \cos \phi_b + 32S^2 J \sin \phi_a \sin \phi_b - 2E_{\mathbf{B}}^b$
$\Gamma'_k(\textcircled{4})$	$8S^2 \Gamma_b + 8S^2 (J_d^z + J_h^z) \cos \phi_a \cos \phi_b + 32S^2 J \sin \phi_a \sin \phi_b - 2E_{\mathbf{B}}^b$
Stripe	
$\Gamma_s(\textcircled{1})$	$4S^2 \Gamma_b + 8S^2 (J_d^z + J_h^z) \cos \phi_a \cos \phi_b + 32S^2 J \sin \phi_a \sin \phi_b - 2E_{\mathbf{B}}^b$
$\Gamma_s(\textcircled{2})$	$4S^2 \Gamma_a + 8S^2 (J_d^z + J_h^z) \cos \phi_a \cos \phi_b + 32S^2 J \sin \phi_a \sin \phi_b - 2E_{\mathbf{B}}^a$
$\Gamma_s(\textcircled{3})$	$4S^2 (\Gamma_a + \Gamma_b) + 4S^2 (J_d^z + 2J_h^z) \cos \phi_a \cos \phi_b + 24S^2 J \sin \phi_a \sin \phi_b - E_{\mathbf{B}}^a - E_{\mathbf{B}}^b$
$\Gamma_s(\textcircled{4})$	$4S^2 (\Gamma_a + \Gamma_b) + 4S^2 (2J_d^z + J_h^z) \cos \phi_a \cos \phi_b + 24S^2 J \sin \phi_a \sin \phi_b - E_{\mathbf{B}}^a - E_{\mathbf{B}}^b$
$\Gamma_s(\textcircled{5})$	$4S^2 (\Gamma_a + \Gamma_b) + 8S^2 (J_d^z + J_h^z) \cos \phi_a \cos \phi_b + 32S^2 J \sin \phi_a \sin \phi_b - E_{\mathbf{B}}^a - E_{\mathbf{B}}^b$

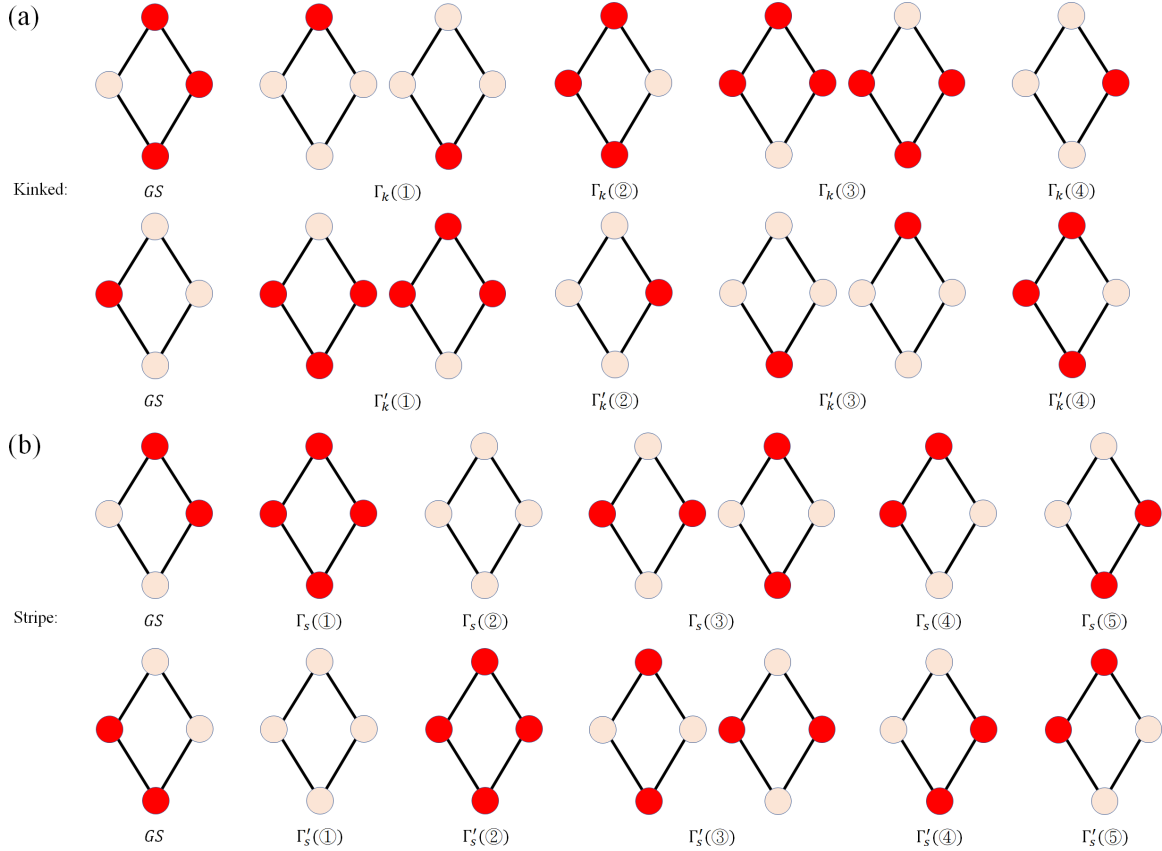


FIG. 5. Possible configurations during the perturbation process for (a) kinked and (b) stripe states. For the ground state there are two configurations in kinked state and thus their evolving must be considered separately. Different configurations that give equal denominator contribution are labeled with the same Γ .

Finally, through considering all possible intermediate processes akin to the one in Fig. 2(b), we obtain the energy correction. For the kinked state,

$$\begin{aligned} \delta E_{\text{kinked}}^{(4)} = & \frac{(J_1^{d(1)})^2 (J_3^{d(2)})^2}{(\Gamma_1)^2 \Gamma_4} + \frac{(J_2^{d(1)})^2 (J_3^{d(2)})^2}{(\Gamma_2)^2 \Gamma_4} \\ & + \frac{(J_3^{d(1)})^2 (J_1^{d(2)})^2}{(\Gamma_3)^2 \Gamma_4} + \frac{(J_3^{d(1)})^2 (J_2^{d(2)})^2}{(\Gamma_3)^2 \Gamma_4} \\ & + \frac{4J_1^{d(1)} J_3^{d(1)} J_1^{d(2)} J_3^{d(2)}}{\Gamma_1 \Gamma_3 \Gamma_k^{(4)}} + \frac{4J_2^{d(1)} J_3^{d(1)} J_2^{d(2)} J_3^{d(2)}}{\Gamma_2 \Gamma_3 \Gamma'_k^{(4)}} \\ & + \frac{2J_1^{d(1)} J_3^{d(1)} J_1^{d(2)} J_3^{d(2)}}{\Gamma_1 \Gamma_3 \Gamma_4} + \frac{2J_2^{d(1)} J_3^{d(1)} J_2^{d(2)} J_3^{d(2)}}{\Gamma_2 \Gamma_3 \Gamma_4}, \end{aligned} \quad (\text{A4})$$

and for stripe state,

$$\begin{aligned} \delta E_{\text{stripe}}^{(4)} = & \frac{2(J_3^{d(1)})^2 J_1^{d(2)} J_2^{d(2)}}{(\Gamma_3)^2 \Gamma_4} + \frac{2J_1^{d(1)} J_2^{d(1)} (J_3^{d(2)})^2}{\Gamma_1 \Gamma_2 \Gamma_4} \\ & + \frac{2(J_3^{d(1)})^2 J_1^{d(2)} J_2^{d(2)}}{(\Gamma_3)^2 \Gamma_5} + \frac{2J_1^{d(1)} J_2^{d(1)} (J_3^{d(2)})^2}{\Gamma_1 \Gamma_2 \Gamma_5} \end{aligned}$$

$$\begin{aligned} & + \frac{2J_1^{d(1)} J_3^{d(1)} J_2^{d(2)} J_3^{d(2)}}{\Gamma_1 \Gamma_3 \Gamma_4} + \frac{2J_2^{d(1)} J_3^{d(1)} J_1^{d(2)} J_3^{d(2)}}{\Gamma_2 \Gamma_3 \Gamma_5} \\ & + \frac{2J_1^{d(1)} J_3^{d(1)} J_2^{d(2)} J_3^{d(2)}}{\Gamma_1 \Gamma_3 \Gamma_5} + \frac{2J_2^{d(1)} J_3^{d(1)} J_1^{d(2)} J_3^{d(2)}}{\Gamma_2 \Gamma_3 \Gamma_4}, \end{aligned} \quad (\text{A5})$$

where $\delta E^{(4)}$ is the energy correction per site. Eqs. (A4) and (A5) will then be used for studying the degeneracy lifting.

APPENDIX B: INFINITE PROJECTED ENTANGLED-PAIR STATE

To study our effective model when the fluctuation is strong, we have no other option but to turn to the assistance of numerical tools. Due to the frustration that hinders the usage of quantum Monte Carlo, we adopt the infinite projected entangled-pair state (iPEPS) [91–93,125] for our purpose. There are two parts for the iPEPS tensor network. One is the tensors within the repeating unit cell, where each composing unit is a rank-5 tensor with four auxiliary bonds (dimension D) and one physical bond representing the size of local Hilbert space (dimension $d = 2$ for $S = 1/2$). Since originally iPEPS was designed for the square lattice, in the triangular lattice the coordinate number for each site is equal to 6. Instead of increasing the number of auxiliary bonds which would make

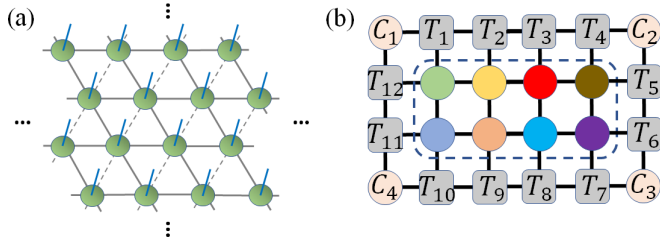


FIG. 6. (a) Composition of the rank-5 tensors into the formation of triangular lattice. Grey solid bonds represent the auxiliary bonds with dimension D , and blue open legs are the local indices with dimension $d = 2$ for the $S = 1/2$ system. Dashed bonds are not the real legs for the tensors but we apply $H_{ij} = \hat{S}_i^+ \hat{S}_j^- + \hat{S}_i^- \hat{S}_j^+$ on these bonds too for simulating the triangular lattice. (b) The double layered tensors with bond dimension D^2 in the bulk, enclosed by the blue dashed box, and the environment tensors. The dimension of bonds interconnecting C and T tensors is labeled by χ , with $\chi \geq D^2$ to guarantee accuracy.

the computation cumbersome, however, we apply the local Hamiltonian also along the virtual bonds [dashed bonds in Fig. 6(a)] when calculating the energy. As a result, the overall lattice structure is effectively equivalent to the triangular lattice.

Another important part for iPEPS lies in the environment tensors. Since the thermodynamics limit can be extrapolated through the corner transfer matrix renormalization group (CTMRG) procedure [126–128], we need to first trace out the physical legs of each tensor with its adjoint one, forming the so-called double layered tensor where each bond is of dimension D^2 . We then adopt the CTMRG, and after the fixed-point tensors have been found they act as the effective “bath” surrounding the bulk tensors, where we label the ones on the corners with C and ones on the edges with T . One example with the bulk size equal to 4×2 is provided in Fig. 6(b).

Last, we need to optimize the tensors so that the overall network can represent the ground state ansatz of the target Hamiltonian. Here we adopt the variational optimization with the usage of automatic differentiation, first introduced by Liao *et al.* [129]. We adopt the widely applicable package, PEPS-TORCH [130], for our calculation. For readers aiming for some further information, we refer to our previous works in Refs. [131,132].

APPENDIX C: CLUSTER MEAN-FIELD THEORY

In this Appendix we briefly introduce the CMFT method that we use for numerically solving Eq. (23). To adopt this method, we first divide our Hamiltonian into two parts: H_C

within the chosen cluster, and $H_{\partial C}$ that contains the terms connecting the bulk to the environment on the boundary of the cluster. H_C possesses the exact form of Eq. (23), and the mean-field decoupling only takes place in $H_{\partial C}$, written as

$$H_{\partial C} = -t \sum'_{ij} (b_i^\dagger \langle b_j \rangle + \text{H.c.}) + \sum'_{ij} V_{ij} n_i \langle n_j \rangle, \quad (\text{C1})$$

where the prime symbol indicates that this summation is between site i on the boundary of the cluster and site j connected to i outside the cluster. Our effective Hamiltonian is then written as $H_{\text{eff}} = H_C + H_{\partial C}$. Although we write down the most general form in Eq. (C1), in this work we apply CMFT for the case with only the nearest-neighbor coupling. We then exactly diagonalize the effective Hamiltonian and obtain the ground state to calculate the mean-field parameters, $\langle b_j \rangle$ and $\langle n_j \rangle$, for the following iteration. After the mean-field parameters converge to consistent values, our calculation reaches its self-consistent solution. In CMFT, exact diagonalizations are performed within the chosen cluster. Therefore, we do not expect to include the long-range entanglement beyond the cluster size. To study this finite size effect and infer the phases in the thermodynamic limit, a common practice is to compute the order parameters at varying cluster sizes and extrapolate to infinity.

CMFT is considered to be more accurate than the regular single-site mean-field theory, in that it can capture the correct correlation within the selected cluster. Thus it is suitable for states whose correlation length is small, meaning that deep inside the ordered phase (or away from transition boundary) we can use CMFT and obtain quite accurate results. Because of the above-mentioned reason, for the boundary lines shown in Fig. 4, we have extrapolated the energies and order parameters for both the first- and second-order transition boundaries to give a better outcome. In addition, due to the randomness from the initialization process, CMFT could converge to distinct phases with the same set of parameters. In this case, one should compare the energies among them to determine the correct ground state. Accordingly, it becomes a challenge when two stable phases appear with energy differences less than or comparable to the finite size effect.

Our CMFT calculation for Eq. (23) provides definitive results on most of the phases shown in Fig. 4. However, it is nontrivial to resolve the ground state phase between the stripe and kinked supersolid due to the fact that the energy difference between these two lies in the fourth-order energy correction from the perturbation theory. For the 4×4 cluster we employed, this difference is comparable to the finite size effect coming from the boundary, as can be estimated by investigating the changes in energy upon displacements of the solid patterns. However, by checking the order parameters we can still diagnose different phases.

- [1] J. Villain, R. Bidaux, J.-P. Carton, and R. Conte, Order as an effect of disorder, *J. Phys. (France)* **41**, 1263 (1980).
 [2] C. L. Henley, Ordering by disorder: Ground-state selection in fcc vector antiferromagnets, *J. Appl. Phys.* **61**, 3962 (1987).

- [3] E. Rastelli and A. Tassi, Competition between thermal and quantum fluctuations in a Heisenberg rhombohedral antiferromagnet, *J. Phys. C* **21**, L35 (1988).
 [4] C. L. Henley, Ordering due to disorder in a frustrated vector antiferromagnet, *Phys. Rev. Lett.* **62**, 2056 (1989).

- [5] P. Chandra, P. Coleman, and A. I. Larkin, Ising transition in frustrated Heisenberg models, *Phys. Rev. Lett.* **64**, 88 (1990).
- [6] A. V. Chubukov and D. I. Golosov, Quantum theory of an antiferromagnet on a triangular lattice in a magnetic field, *J. Phys.: Condens. Matter* **3**, 69 (1991).
- [7] J. T. Chalker, P. C. W. Holdsworth, and E. F. Shender, Hidden order in a frustrated system: Properties of the Heisenberg kagomé antiferromagnet, *Phys. Rev. Lett.* **68**, 855 (1992).
- [8] Q. Sheng and C. L. Henley, Ordering due to disorder in a triangular Heisenberg antiferromagnet with exchange anisotropy, *J. Phys.: Condens. Matter* **4**, 2937 (1992).
- [9] T. Yildirim, A. B. Harris, and E. F. Shender, Three-dimensional ordering in bct antiferromagnets due to quantum disorder, *Phys. Rev. B* **53**, 6455 (1996).
- [10] R. Moessner and J. T. Chalker, Low-temperature properties of classical geometrically frustrated antiferromagnets, *Phys. Rev. B* **58**, 12049 (1998).
- [11] M. E. Zhitomirsky, A. Honecker, and O. A. Petrenko, Field induced ordering in highly frustrated antiferromagnets, *Phys. Rev. Lett.* **85**, 3269 (2000).
- [12] D. Bergman, J. Alicea, E. Gull, S. Trebst, and L. Balents, Order-by-disorder and spiral spin-liquid in frustrated diamond-lattice antiferromagnets, *Nat. Phys.* **3**, 487 (2007).
- [13] J.-S. Bernier, M. J. Lawler, and Y. B. Kim, Quantum order by disorder in frustrated diamond lattice antiferromagnets, *Phys. Rev. Lett.* **101**, 047201 (2008).
- [14] M. E. Zhitomirsky, M. V. Gvozdkova, P. C. W. Holdsworth, and R. Moessner, Quantum order by disorder and accidental soft mode in $\text{Er}_2\text{Ti}_2\text{O}_7$, *Phys. Rev. Lett.* **109**, 077204 (2012).
- [15] S. B. Lee, E. K.-H. Lee, A. Paramekanti, and Y. B. Kim, Order-by-disorder and magnetic field response in the Heisenberg-Kitaev model on a hyperhoneycomb lattice, *Phys. Rev. B* **89**, 014424 (2014).
- [16] A. L. Chernyshev and M. E. Zhitomirsky, Quantum selection of order in an XXZ antiferromagnet on a kagome lattice, *Phys. Rev. Lett.* **113**, 237202 (2014).
- [17] B. Javanparast, A. G. R. Day, Z. Hao, and M. J. P. Gingras, Order-by-disorder near criticality in XY pyrochlore magnets, *Phys. Rev. B* **91**, 174424 (2015).
- [18] G. Jackeli and A. Avella, Quantum order by disorder in the Kitaev model on a triangular lattice, *Phys. Rev. B* **92**, 184416 (2015).
- [19] I. Rousochatzakis, J. Reuther, R. Thomale, S. Rachel, and N. B. Perkins, Phase diagram and quantum order by disorder in the Kitaev $K_1 - K_2$ honeycomb magnet, *Phys. Rev. X* **5**, 041035 (2015).
- [20] J. G. Rau, S. Petit, and M. J. P. Gingras, Order by virtual crystal field fluctuations in pyrochlore XY antiferromagnets, *Phys. Rev. B* **93**, 184408 (2016).
- [21] B. Danu, G. Nambiar, and R. Ganesh, Extended degeneracy and order by disorder in the square lattice $J_1 - J_2 - J_3$ model, *Phys. Rev. B* **94**, 094438 (2016).
- [22] J. G. Rau, P. A. McClarty, and R. Moessner, Pseudo-Goldstone gaps and order-by-quantum disorder in frustrated magnets, *Phys. Rev. Lett.* **121**, 237201 (2018).
- [23] L. Savary and L. Balents, Quantum spin liquids: A review, *Rep. Prog. Phys.* **80**, 016502 (2017).
- [24] Y. Zhou, K. Kanoda, and T.-K. Ng, Quantum spin liquid states, *Rev. Mod. Phys.* **89**, 025003 (2017).
- [25] S.-J. Dong, W. Liu, X.-F. Zhou, G.-C. Guo, Z.-W. Zhou, Y.-J. Han, and L. He, Peculiar supersolid phases induced by frustrated tunneling in the extended Bose-Hubbard model, *Phys. Rev. B* **96**, 045119 (2017).
- [26] W.-L. Tu, H.-K. Wu, and T. Suzuki, Frustration-induced super-solid phases of extended Bose-Hubbard model in the hard-core limit, *J. Phys.: Condens. Matter* **32**, 455401 (2020).
- [27] M. J. Harris, S. T. Bramwell, D. F. McMorrow, T. Zeiske, and K. W. Godfrey, Geometrical frustration in the ferromagnetic pyrochlore $\text{Ho}_2\text{Ti}_2\text{O}_7$, *Phys. Rev. Lett.* **79**, 2554 (1997).
- [28] S. T. Bramwell and M. J. P. Gingras, Spin ice state in frustrated magnetic pyrochlore materials, *Science* **294**, 1495 (2001).
- [29] A. Eckardt, P. Hauke, P. Soltan-Panahi, C. Becker, K. Sengstock, and M. Lewenstein, Frustrated quantum antiferromagnetism with ultracold bosons in a triangular lattice, *Europhys. Lett.* **89**, 10010 (2010).
- [30] C. Becker, P. Soltan-Panahi, J. Kronjäger, S. Dörscher, K. Bongs, and K. Sengstock, Ultracold quantum gases in triangular optical lattices, *New J. Phys.* **12**, 065025 (2010).
- [31] J. Struck, C. Ölschläger, R. Le Targat, P. Soltan-Panahi, A. Eckardt, M. Lewenstein, P. Windpassinger, and K. Sengstock, Quantum simulation of frustrated classical magnetism in triangular optical lattices, *Science* **333**, 996 (2011).
- [32] O. A. Starykh, Unusual ordered phases of highly frustrated magnets: A review, *Rep. Prog. Phys.* **78**, 052502 (2015).
- [33] Y. I. Dublennykh, Ground states of the Ising model on an anisotropic triangular lattice: Stripes and zigzags, *J. Phys.: Condens. Matter* **25**, 406003 (2013).
- [34] Y. Han, Y. Shokef, A. M. Alsayed, P. Yunker, T. C. Lubensky, and A. G. Yodh, Geometric frustration in buckled colloidal monolayers, *Nature (London)* **456**, 898 (2008).
- [35] Y. Shokef and T. C. Lubensky, Stripes, zigzags, and slow dynamics in buckled hard spheres, *Phys. Rev. Lett.* **102**, 048303 (2009).
- [36] Y. Shokef, A. Souslov, and T. C. Lubensky, Order by disorder in the antiferromagnetic Ising model on an elastic triangular lattice, *Proc. Natl. Acad. Sci. USA* **108**, 11804 (2011).
- [37] R. Schick, T. Ziman, and M. E. Zhitomirsky, Quantum versus thermal fluctuations in the fcc antiferromagnet: Alternative routes to order by disorder, *Phys. Rev. B* **102**, 220405(R) (2020).
- [38] R. Stebbings and F. Dunning, *Rydberg States of Atoms and Molecules*, Essays in Nuclear Astrophysics (Cambridge University Press, Cambridge, 1983).
- [39] T. Gallagher, *Rydberg Atoms*, Cambridge Monographs on Atomic, Molecular and Chemical Physics (Cambridge University Press, Cambridge, 1994).
- [40] M. Saffman, T. G. Walker, and K. Mølmer, Quantum information with Rydberg atoms, *Rev. Mod. Phys.* **82**, 2313 (2010).
- [41] X. Wu, X. Liang, Y. Tian, F. Yang, C. Chen, Y.-C. Liu, M. K. Tey, and L. You, A concise review of Rydberg atom based quantum computation and quantum simulation, *Chin. Phys. B* **30**, 020305 (2021).
- [42] G. Semeghini, H. Levine, A. Keesling, S. Ebadi, T. T. Wang, D. Bluvstein, R. Verresen, H. Pichler, M. Kalinowski, R. Samajdar, A. Omran, S. Sachdev, A. Vishwanath, M. Greiner, V. Vuletić, and M. D. Lukin, Probing topological spin liquids on a programmable quantum simulator, *Science* **374**, 1242 (2021).

- [43] A. J. Daley, I. Bloch, C. Kokail, N. Pearson, M. Troyer, and P. Zoller, Practical quantum advantage in quantum simulation, *Nature (London)* **607**, 667 (2022).
- [44] R. Samajdar, W. W. Ho, H. Pichler, M. D. Lukin, and S. Sachdev, Quantum phases of Rydberg atoms on a kagome lattice, *Proc. Natl. Acad. Sci. USA* **118**, e2015785118 (2021).
- [45] D. Jaksch, J. I. Cirac, P. Zoller, S. L. Rolston, R. Côté, and M. D. Lukin, Fast quantum gates for neutral atoms, *Phys. Rev. Lett.* **85**, 2208 (2000).
- [46] M. D. Lukin, M. Fleischhauer, R. Cote, L. M. Duan, D. Jaksch, J. I. Cirac, and P. Zoller, Dipole blockade and quantum information processing in mesoscopic atomic ensembles, *Phys. Rev. Lett.* **87**, 037901 (2001).
- [47] A. P. n. Orioli, A. Signoles, H. Wildhagen, G. Günter, J. Berges, S. Whitlock, and M. Weidemüller, Relaxation of an isolated dipolar-interacting Rydberg quantum spin system, *Phys. Rev. Lett.* **120**, 063601 (2018).
- [48] S. de Léséleuc, V. Lienhard, P. Scholl, D. Barredo, S. Weber, N. Lang, H. P. Büchler, T. Lahaye, and A. Browaeys, Observation of a symmetry-protected topological phase of interacting bosons with Rydberg atoms, *Science* **365**, 775 (2019).
- [49] Y. Chew, T. Tomita, T. P. Mahesh, S. Sugawa, S. de Léséleuc, and K. Ohmori, Ultrafast energy exchange between two single Rydberg atoms on a nanosecond timescale, *Nat. Photon.* **16**, 724 (2022).
- [50] A. Signoles, T. Franz, R. Ferracini Alves, M. Gärtner, S. Whitlock, G. Zürn, and M. Weidemüller, Glassy dynamics in a disordered Heisenberg quantum spin system, *Phys. Rev. X* **11**, 011011 (2021).
- [51] P. Scholl, H. J. Williams, G. Bornet, F. Wallner, D. Barredo, L. Henriot, A. Signoles, C. Hainaut, T. Franz, S. Geier, A. Tebben, A. Salzinger, G. Zürn, T. Lahaye, M. Weidemüller, and A. Browaeys, Microwave engineering of programmable XXZ Hamiltonians in arrays of Rydberg atoms, *PRX Quantum* **3**, 020303 (2022).
- [52] S. Geier, N. Thaçharoen, C. Hainaut, T. Franz, A. Salzinger, A. Tebben, D. Grimshandl, G. Zürn, and M. Weidemüller, Floquet Hamiltonian engineering of an isolated many-body spin system, *Science* **374**, 1149 (2021).
- [53] I. Bloch, J. Dalibard, and W. Zwerger, Many-body physics with ultracold gases, *Rev. Mod. Phys.* **80**, 885 (2008).
- [54] I. Bloch, J. Dalibard, and S. Nascimbène, Quantum simulations with ultracold quantum gases, *Nat. Phys.* **8**, 267 (2012).
- [55] P. Windpassinger and K. Sengstock, Engineering novel optical lattices, *Rep. Prog. Phys.* **76**, 086401 (2013).
- [56] M. Tomza, K. Jachymski, R. Gerritsma, A. Negretti, T. Calarco, Z. Idziaszek, and P. S. Julienne, Cold hybrid ion-atom systems, *Rev. Mod. Phys.* **91**, 035001 (2019).
- [57] L. Tanzi, E. Lucioni, F. Famà, J. Catani, A. Fioretti, C. Gabbanini, R. N. Bisset, L. Santos, and G. Modugno, Observation of a dipolar quantum gas with metastable supersolid properties, *Phys. Rev. Lett.* **122**, 130405 (2019).
- [58] F. Böttcher, J.-N. Schmidt, M. Wenzel, J. Hertkorn, M. Guo, T. Langen, and T. Pfau, Transient supersolid properties in an array of dipolar quantum droplets, *Phys. Rev. X* **9**, 011051 (2019).
- [59] L. Chomaz, D. Petter, P. Ilzhöfer, G. Natale, A. Trautmann, C. Politi, G. Durastante, R. M. W. van Bijnen, A. Patscheider, M. Sohmen, M. J. Mark, and F. Ferlaino, Long-lived and transient supersolid behaviors in dipolar quantum gases, *Phys. Rev. X* **9**, 021012 (2019).
- [60] G. Natale, R. M. W. van Bijnen, A. Patscheider, D. Petter, M. J. Mark, L. Chomaz, and F. Ferlaino, Excitation spectrum of a trapped dipolar supersolid and its experimental evidence, *Phys. Rev. Lett.* **123**, 050402 (2019).
- [61] L. Tanzi, S. M. Rocuzzo, E. Lucioni, F. Famà, A. Fioretti, C. Gabbanini, G. Modugno, A. Recati, and S. Stringari, Supersolid symmetry breaking from compressional oscillations in a dipolar quantum gas, *Nature (London)* **574**, 382 (2019).
- [62] J. Schachenmayer, I. Lesanovsky, A. Micheli, and A. J. Daley, Dynamical crystal creation with polar molecules or Rydberg atoms in optical lattices, *New J. Phys.* **12**, 103044 (2010).
- [63] A. V. Gorshkov, S. R. Manmana, G. Chen, J. Ye, E. Demler, M. D. Lukin, and A. M. Rey, Tunable superfluidity and quantum magnetism with ultracold polar molecules, *Phys. Rev. Lett.* **107**, 115301 (2011).
- [64] A. V. Gorshkov, S. R. Manmana, G. Chen, E. Demler, M. D. Lukin, and A. M. Rey, Quantum magnetism with polar alkali-metal dimers, *Phys. Rev. A* **84**, 033619 (2011).
- [65] B. Yan, S. A. Moses, B. Gadway, J. P. Covey, K. R. A. Hazzard, A. M. Rey, D. S. Jin, and J. Ye, Observation of dipolar spin-exchange interactions with lattice-confined polar molecules, *Nature (London)* **501**, 521 (2013).
- [66] K. R. A. Hazzard, B. Gadway, M. Foss-Feig, B. Yan, S. A. Moses, J. P. Covey, N. Y. Yao, M. D. Lukin, J. Ye, D. S. Jin, and A. M. Rey, Many-body dynamics of dipolar molecules in an optical lattice, *Phys. Rev. Lett.* **113**, 195302 (2014).
- [67] S. Baier, M. J. Mark, D. Petter, K. Aikawa, L. Chomaz, Z. Cai, M. Baranov, P. Zoller, and F. Ferlaino, Extended Bose-Hubbard models with ultracold magnetic atoms, *Science* **352**, 201 (2016).
- [68] L. Chomaz, I. Ferrier-Barbut, F. Ferlaino, B. Laburthe-Tolra, B. L. Lev, and T. Pfau, Dipolar physics: A review of experiments with magnetic quantum gases, *Rep. Prog. Phys.* **86**, 026401 (2023).
- [69] L. Su, A. Douglas, M. Szurek, R. Groth, S. F. Ozturk, A. Krahn, A. H. Hébert, G. A. Phelps, S. Ebadi, S. Dickerson, F. Ferlaino, O. Marković, and M. Greiner, Dipolar quantum solids emerging in a Hubbard quantum simulator, *Nature (London)* **622**, 724 (2023).
- [70] T. Chanda, L. Barbiero, M. Lewenstein, M. J. Mark, and J. Zakrzewski, Recent progress on quantum simulations of non-standard Bose-Hubbard models, [arXiv:2405.07775](https://arxiv.org/abs/2405.07775).
- [71] B. Capogrosso-Sansone, C. Trefzger, M. Lewenstein, P. Zoller, and G. Pupillo, Quantum phases of cold polar molecules in 2D optical lattices, *Phys. Rev. Lett.* **104**, 125301 (2010).
- [72] T. Ohgoe, T. Suzuki, and N. Kawashima, Novel mechanism of supersolid of ultracold polar molecules in optical lattices, *J. Phys. Soc. Jpn.* **80**, 113001 (2011).
- [73] D. Yamamoto, I. Danshita, and C. A. R. Sá de Melo, Dipolar bosons in triangular optical lattices: Quantum phase transitions and anomalous hysteresis, *Phys. Rev. A* **85**, 021601(R) (2012).
- [74] D. Yamamoto, G. Marmorini, and I. Danshita, Quantum phase diagram of the triangular-lattice XXZ model in a magnetic field, *Phys. Rev. Lett.* **112**, 127203 (2014).
- [75] T. Ohgoe, T. Suzuki, and N. Kawashima, Quantum phases of hard-core bosons on two-dimensional lattices with anisotropic dipole-dipole interaction, *Phys. Rev. A* **86**, 063635 (2012).

- [76] C. Zhang, A. Safavi-Naini, A. M. Rey, and B. Capogrosso-Sansone, Equilibrium phases of tilted dipolar lattice bosons, *New J. Phys.* **17**, 123014 (2015).
- [77] H.-K. Wu and W.-L. Tu, Competing quantum phases of hardcore bosons with tilted dipole-dipole interaction, *Phys. Rev. A* **102**, 053306 (2020).
- [78] C. Zhang, J. Zhang, J. Yang, and B. Capogrosso-Sansone, Ground states of two-dimensional tilted dipolar bosons with density-induced hopping, *Phys. Rev. A* **103**, 043333 (2021).
- [79] R. Kaneko and I. Danshita, Tensor-network study of correlation-spreading dynamics in the two-dimensional Bose-Hubbard model, *Commun. Phys.* **5**, 65 (2022).
- [80] M. Hughes and D. Jaksch, Dipolar Bose-Hubbard model in finite-size real-space cylindrical lattices, *Phys. Rev. A* **105**, 053301 (2022).
- [81] J. Zhang, C. Zhang, J. Yang, and B. Capogrosso-Sansone, Supersolid phases of lattice dipoles tilted in three dimensions, *Phys. Rev. A* **105**, 063302 (2022).
- [82] P. H. Nguyen and M. Boninsegni, Phase diagram of hard core bosons with anisotropic interactions, *J. Low Temp. Phys.* **209**, 34 (2022).
- [83] S. Bandyopadhyay, H. Sable, D. Gaur, R. Bai, S. Mukerjee, and D. Angom, Quantum phases of dipolar bosons in a multi-layer optical lattice, *Phys. Rev. A* **106**, 043301 (2022).
- [84] Y. Hebib, C. Zhang, J. Yang, and B. Capogrosso-Sansone, Quantum phases of lattice dipolar bosons coupled to a high-finesse cavity, *Phys. Rev. A* **107**, 043318 (2023).
- [85] P. R. N. Falcão and J. Zakrzewski, Nonergodic dynamics for an impurity interacting with bosons in a tilted lattice, *Phys. Rev. B* **108**, 134201 (2023).
- [86] M. W. Long, Effects that can stabilise multiple spin-density waves, *J. Phys.: Condens. Matter* **1**, 2857 (1989).
- [87] M. T. Heinilä and A. S. Oja, Selection of the ground state in type-I fcc antiferromagnets in an external magnetic field, *Phys. Rev. B* **48**, 7227 (1993).
- [88] M. E. Zhitomirsky, Real-space perturbation theory for frustrated magnets: Application to magnetization plateaus, *J. Phys.: Conf. Ser.* **592**, 012110 (2015).
- [89] I. Rousochatzakis and N. B. Perkins, Classical spin liquid instability driven by off-diagonal exchange in strong spin-orbit magnets, *Phys. Rev. Lett.* **118**, 147204 (2017).
- [90] B. Placke, R. Moessner, and O. Benton, Hierarchy of energy scales and field-tunable order by disorder in dipolar-octupolar pyrochlores, *Phys. Rev. B* **102**, 245102 (2020).
- [91] J. Jordan, R. Orús, G. Vidal, F. Verstraete, and J. I. Cirac, Classical simulation of infinite-size quantum lattice systems in two spatial dimensions, *Phys. Rev. Lett.* **101**, 250602 (2008).
- [92] R. Orús, Tensor networks for complex quantum systems, *Nat. Rev. Phys.* **1**, 538 (2019).
- [93] J. I. Cirac, D. Pérez-García, N. Schuch, and F. Verstraete, Matrix product states and projected entangled pair states: Concepts, symmetries, theorems, *Rev. Mod. Phys.* **93**, 045003 (2021).
- [94] H. Bernien, S. Schwartz, A. Keesling, H. Levine, A. Omran, H. Pichler, S. Choi, A. S. Zibrov, M. Endres, M. Greiner, V. Vuletić, and M. D. Lukin, Probing many-body dynamics on a 51-atom quantum simulator, *Nature (London)* **551**, 579 (2017).
- [95] V. Lienhard, S. de Léséleuc, D. Barredo, T. Lahaye, A. Browaeys, M. Schuler, L.-P. Henry, and A. M. Läuchli, Observing the space- and time-dependent growth of correlations in dynamically tuned synthetic Ising models with antiferromagnetic interactions, *Phys. Rev. X* **8**, 021070 (2018).
- [96] S. Ebadi, T. T. Wang, H. Levine, A. Keesling, G. Semeghini, A. Omran, D. Bluvstein, R. Samajdar, H. Pichler, W. W. Ho, S. Choi, S. Sachdev, M. Greiner, V. Vuletić, and M. D. Lukin, Quantum phases of matter on a 256-atom programmable quantum simulator, *Nature (London)* **595**, 227 (2021).
- [97] M. Saffman, Quantum computing with atomic qubits and Rydberg interactions: Progress and challenges, *J. Phys. B: At. Mol. Opt. Phys.* **49**, 202001 (2016).
- [98] J. M. Raimond, M. Brune, and S. Haroche, Manipulating quantum entanglement with atoms and photons in a cavity, *Rev. Mod. Phys.* **73**, 565 (2001).
- [99] D. Kleppner, Inhibited spontaneous emission, *Phys. Rev. Lett.* **47**, 233 (1981).
- [100] R. G. Hulet, E. S. Hilfer, and D. Kleppner, Inhibited spontaneous emission by a Rydberg atom, *Phys. Rev. Lett.* **55**, 2137 (1985).
- [101] T. L. Nguyen, J. M. Raimond, C. Sayrin, R. Cortiñas, T. Cantat-Moltrecht, F. Assemat, I. Dotsenko, S. Gleyzes, S. Haroche, G. Roux, T. Jolicœur, and M. Brune, Towards quantum simulation with circular Rydberg atoms, *Phys. Rev. X* **8**, 011032 (2018).
- [102] H. Wu, R. Richaud, J.-M. Raimond, M. Brune, and S. Gleyzes, Millisecond-lived circular Rydberg atoms in a room-temperature experiment, *Phys. Rev. Lett.* **130**, 023202 (2023).
- [103] F. Meinert, C. Hölzl, M. A. Nebioglu, A. D'Arnese, P. Karl, M. Dressel, and M. Scheffler, Indium tin oxide films meet circular Rydberg atoms: Prospects for novel quantum simulation schemes, *Phys. Rev. Res.* **2**, 023192 (2020).
- [104] S. R. Cohen and J. D. Thompson, Quantum computing with circular Rydberg atoms, *PRX Quantum* **2**, 030322 (2021).
- [105] T. G. Walker and M. Saffman, Consequences of Zeeman degeneracy for the van der Waals blockade between Rydberg atoms, *Phys. Rev. A* **77**, 032723 (2008).
- [106] X.-F. Shi, Quantum logic and entanglement by neutral Rydberg atoms: Methods and fidelity, *Quantum Sci. Technol.* **7**, 023002 (2022).
- [107] A. Reinhard, T. C. Liebisch, B. Knuffman, and G. Raithel, Level shifts of rubidium Rydberg states due to binary interactions, *Phys. Rev. A* **75**, 032712 (2007).
- [108] A. A. Kamenski, N. L. Manakov, S. N. Mokhnenko, and V. D. Ovsiannikov, Energy of van der Waals and dipole-dipole interactions between atoms in Rydberg states, *Phys. Rev. A* **96**, 032716 (2017).
- [109] T. G. Walker and M. Saffman, Zeros of Rydberg–Rydberg Förster interactions, *J. Phys. B: At., Mol. Opt. Phys.* **38**, S309 (2005).
- [110] S. Ravets, H. Labuhn, D. Barredo, L. Béguin, T. Lahaye, and A. Browaeys, Coherent dipole–dipole coupling between two single Rydberg atoms at an electrically-tuned Förster resonance, *Nat. Phys.* **10**, 914 (2014).
- [111] R. G. Cortiñas, M. Favier, B. Ravon, P. Méhaignerie, Y. Machu, J. M. Raimond, C. Sayrin, and M. Brune, Laser trapping of circular Rydberg atoms, *Phys. Rev. Lett.* **124**, 123201 (2020).

- [112] R. Cardman and G. Raithel, Circularizing Rydberg atoms with time-dependent optical traps, *Phys. Rev. A* **101**, 013434 (2020).
- [113] A. M. Kaufman and K.-K. Ni, Quantum science with optical tweezer arrays of ultracold atoms and molecules, *Nat. Phys.* **17**, 1324 (2021).
- [114] B. Ravon, P. Méhaignerie, Y. Machu, A. D. Hernández, M. Favier, J. M. Raimond, M. Brune, and C. Sayrin, Array of individual circular Rydberg atoms trapped in optical tweezers, *Phys. Rev. Lett.* **131**, 093401 (2023).
- [115] C. Hölzl, A. Götzelmann, E. Pultinevicius, M. Wirth, and F. Meinert, Long-lived circular Rydberg qubits of alkaline-earth atoms in optical tweezers, *Phys. Rev. X* **14**, 021024 (2024).
- [116] Y. Takahashi, Quantum simulation of quantum many-body systems with ultracold two-electron atoms in an optical lattice, *Proc. Jpn. Acad. Ser. B* **98**, 141 (2022).
- [117] A. Chotia, B. Neyenhuis, S. A. Moses, B. Yan, J. P. Covey, M. Foss-Feig, A. M. Rey, D. S. Jin, and J. Ye, Long-lived dipolar molecules and Feshbach molecules in a 3D optical lattice, *Phys. Rev. Lett.* **108**, 080405 (2012).
- [118] S. A. Moses, J. P. Covey, M. T. Miecnikowski, B. Yan, B. Gadway, J. Ye, and D. S. Jin, Creation of a low-entropy quantum gas of polar molecules in an optical lattice, *Science* **350**, 659 (2015).
- [119] L. R. Liu, J. D. Hood, Y. Yu, J. T. Zhang, K. Wang, Y.-W. Lin, T. Rosenband, and K.-K. Ni, Molecular assembly of ground-state cooled single atoms, *Phys. Rev. X* **9**, 021039 (2019).
- [120] L. Anderegg, L. W. Cheuk, Y. Bao, S. Burchesky, W. Ketterle, K.-K. Ni, and J. M. Doyle, An optical tweezer array of ultracold molecules, *Science* **365**, 1156 (2019).
- [121] T. Lahaye, C. Menotti, L. Santos, M. Lewenstein, and T. Pfau, The physics of dipolar bosonic quantum gases, *Rep. Prog. Phys.* **72**, 126401 (2009).
- [122] J. A. Koziol, A. Duft, G. Morigi, and K. P. Schmidt, Systematic analysis of crystalline phases in bosonic lattice models with algebraically decaying density-density interactions, *SciPost Phys.* **14**, 136 (2023).
- [123] See <https://github.com/QuEraComputing/quera-education> for some educational materials.
- [124] D. Zhou, F. Wang, B. Li, X. Lou, and Y. Han, Glassy spin dynamics in geometrically frustrated buckled colloidal crystals, *Phys. Rev. X* **7**, 021030 (2017).
- [125] Y. Motoyama, T. Okubo, K. Yoshimi, S. Morita, T. Kato, and N. Kawashima, TeNeS: Tensor network solver for quantum lattice systems, *Comput. Phys. Commun.* **279**, 108437 (2022).
- [126] T. Nishino and K. Okunishi, Corner transfer matrix renormalization group method, *J. Phys. Soc. Jpn.* **65**, 891 (1996).
- [127] R. Orús and G. Vidal, Simulation of two-dimensional quantum systems on an infinite lattice revisited: Corner transfer matrix for tensor contraction, *Phys. Rev. B* **80**, 094403 (2009).
- [128] P. Corboz, T. M. Rice, and M. Troyer, Competing states in the t - J model: Uniform d -wave state versus stripe state, *Phys. Rev. Lett.* **113**, 046402 (2014).
- [129] H.-J. Liao, J.-G. Liu, L. Wang, and T. Xiang, Differentiable programming tensor networks, *Phys. Rev. X* **9**, 031041 (2019).
- [130] J. Hasik, G. B. Mbeng, W.-L. Tu, and S.-S. Diop, A tensor network library for two-dimensional lattice models, <https://github.com/jurajHasik/peps-torch>, 2020.
- [131] W.-L. Tu, E.-G. Moon, K.-W. Lee, W. E. Pickett, and H.-Y. Lee, Field-induced Bose-Einstein condensation and supersolid in the two-dimensional Kondo necklace, *Commun. Phys.* **5**, 130 (2022).
- [132] W.-L. Tu, X. Lyu, S. R. Ghazanfari, H.-K. Wu, H.-Y. Lee, and N. Kawashima, Cubic ferromagnet and emergent $U(1)$ symmetry on its phase boundary, *Phys. Rev. B* **107**, 224406 (2023).